

An exploratory study on helium mobility in amorphous and crystallized bulk metallic glasses

J. Brechtl^{a,b,*}, S. Agarwal^c, X. Hu^b, D. Chen^d, M. Chancey^d, H. Bei^b, Y.Q. Wang^d, S.J. Zinkle^{b,c,**}

^a The Bredeesen Center for Interdisciplinary Research and Graduate Education, University of Tennessee, Knoxville, TN 37996, USA

^b Materials Science and Technology Division, Oak Ridge National Laboratory, Oak Ridge, TN 37831, USA

^c Department of Nuclear Engineering, University of Tennessee, Knoxville, TN 37996, USA

^d Materials Science and Technology Division, Los Alamos National Laboratory, Los Alamos, NM 87545, USA

ARTICLE INFO

Article history:

Received 25 May 2020

Revised 23 September 2020

Accepted 19 October 2020

Available online 23 October 2020

Keywords:

Bulk metallic glasses

Helium mobility

Nuclear Reaction Analysis

Thermal Desorption Spectroscopy

ABSTRACT

Zr_{52.5}Cu_{17.9}Ni_{14.6}Al₁₀Ti₅ and Cu₆₀Zr₂₀Hf₁₀Ti₁₀ amorphous and crystallized bulk metallic glasses (BMGs) were implanted at room temperature by 150 keV ³He⁺ ions to fluences of 2×10^{15} cm⁻² and 5×10^{15} cm⁻², producing peak implanted He concentrations of ~1,100 and 3,500 appm, respectively. Nuclear reaction analysis (NRA) performed on post-implantation annealed samples at various temperatures between 250 and 600 °C (~0.30 to 0.75 of the absolute melting temperature T_m of the BMGs) revealed no appreciable He migration. Complementary thermal desorption spectroscopy (TDS) on as-implanted samples, which involved in situ annealing, showed appreciable He release only at temperatures higher than ~700 °C (~0.76–0.90 T_m) in all the samples. Half or more of the implanted He did not desorb up to the maximum investigated TDS annealing temperature of 770 °C (~0.85–0.97 T_m). The lack of pronounced He diffusion up to 600 °C as observed from the NRA and TDS data was attributed to He trapping in free volume sites present in the BMGs, which seems to play a similar role to vacancies in crystalline materials. It was also observed that in both the amorphous and crystallized forms of the Zr BMG, the sample implanted to the lower fluence released more He as compared to the sample implanted with a higher fluence. The crystalline forms of both the Cu and Zr BMGs released more He as compared to their amorphous counterparts.

© 2020 Elsevier B.V. All rights reserved.

1. Introduction

The future of global fusion energy will be largely dependent on the development of high-performance, reduced activation materials [1–5]. Currently, one of the major impediments for materials in fusion environments involves helium retention. Helium, when trapped in a material over time, can lead to deleterious effects such as embrittlement and swelling. The swelling that occurs is due to the formation of He-containing cavities due to the extremely low solubility of He [6]. In crystalline materials, this is especially an issue since the inert gas can induce pronounced swelling and/or become trapped at grain boundaries, severely weakening the material through embrittlement. However, materials which are amorphous in nature, such as bulk metallic glasses (BMGs), lack grain boundaries. The absence of grain boundary helium traps combined with

their high strength and elastic deformability [7–9], therefore, make BMGs a potentially viable material in nuclear fusion environments.

It is believed that a factor which may make amorphous metals highly desirable for use in different components of a fusion reactor is their potentially high helium permeability due to their large free atomic volume and lack of grain boundaries which can act as helium traps [10]. Indeed, Su et al. have reported high He permeability in SiOC amorphous samples during room temperature He implantation [11,12]. Therefore, metallic glasses have a potential advantage over crystalline materials since He retention may be low, leading to a better resistance to cavity swelling and embrittlement at elevated temperatures. Also, if a high density of cavities is not present, the amount of tritium trapped in the BMG under prototypic fusion reactor conditions might also be very low [13]. Therefore, it has been suggested that BMGs could be a viable candidate for use in fusion energy systems as piping, window, or diagnostic sensor components.

In recent studies, BMGs showed higher resistance to He damage as compared to common crystalline fusion materials such as W.

* Corresponding author.

** Co-corresponding author.

E-mail addresses: jbrechtl@vols.utk.edu (J. Brechtl), szinkle@utk.edu (S.J. Zinkle).

For example, a study by Mei et al. found that $(\text{Cu}_{47}\text{Zr}_{45}\text{Al}_8)_{98.5}\text{Y}_{1.5}$ BMG showed superior radiation resistance as compared to polycrystalline W during 500 keV He irradiation at room temperature to fluences of 2×10^{17} ions/cm², 1×10^{18} ions/cm², and 2×10^{18} ions/cm² [14]. Scanning electron microscopy (SEM) showed that surface peeling and delamination occurred in the W alloy during irradiation whereas the BMG only exhibited slight damage at depths within the ion range. Furthermore, X-ray diffraction (XRD) patterns revealed that the BMG specimens did not crystallize under any irradiation condition. In a comparable study, Wang et al. [15] examined the irradiation response of $\text{Zr}_{64}\text{Cu}_{17.8}\text{Ni}_{10.7}\text{Al}_{7.5}$, $(\text{Cu}_{47}\text{Zr}_{45}\text{Al}_8)_{98.5}\text{Y}_{1.5}$, and $\text{Co}_{61.2}\text{B}_{26.2}\text{Si}_{7.8}\text{Ta}_{4.8}$ BMGs, and W alloy after exposure to the same irradiation conditions as the investigation described in [14]. All the BMGs retained their amorphous structure under all irradiation fluences, as indicated by the corresponding XRD patterns. Furthermore, the results showed that all the BMGs displayed greater resistance to He damage as compared to the W alloy. Within the studied BMGs, the Zr and Cu based BMGs demonstrated better resistance than the Co based BMG. The greater degree of damage in the W and Co based BMG alloys corresponded to an appreciable amount of surface degradation caused by He embrittlement.

Previous studies have also investigated the effects of helium bombardment on the microstructure of metallic glasses [16–19,54]. One important study found that helium implanted $\text{Ni}_{73}\text{P}_{27}$ nanocylinders (~130 nm diameter) exhibited improved ductility with no sacrifice in yield and ultimate tensile strengths [19]. The nano-cylinders were implanted with He^+ at energies of 50, 100, 150, and 200 keV, to create a uniform helium concentration of ~3 at. % throughout the nano-cylinders. Transmission electron microscopy (TEM) imaging and through-focus analysis revealed that the specimens contained ~2 nm helium bubbles distributed uniformly throughout the nano-cylinder volume. In-situ tensile experiments indicated that helium-implanted specimens exhibited enhanced ductility as evidenced by a 2-fold increase in plastic strain over as-fabricated specimens, with no sacrifice in yield and ultimate tensile strengths. This improvement in mechanical properties suggests that metallic glasses may actually exhibit a favorable response to high levels of helium implantation.

Despite the efforts to examine the microstructural behavior of He in metallic glasses, there are limited publications regarding the diffusion of helium in bulk amorphous alloys and their crystalline counterparts. Recent studies on amorphous silicon oxycarbide by Su et al. reported very high helium permeability even at room temperature [11,12]. Conversely, some other studies have reported low He permeability in He-implanted Ni-based amorphous alloys for implantation fluences of 1 to $5 \times 10^{20}/\text{m}^2$ [20]. Through this study, we are trying to investigate the role of different microstructures and BMG compositions on He diffusion by performing the He implantation and post-irradiation anneals on amorphous BMGs and their crystalline counterparts. The effect of fluence (implanted He concentration) on the He diffusion in both amorphous and crystallized BMGs was also examined. For this work, He was implanted using an ion implanter for two different fluence values. He diffusion was investigated using nuclear reaction analysis (NRA) and total He-retention was studied using thermal desorption spectroscopy (TDS). The He induced microstructure was investigated using XRD and TEM techniques.

2. Experimental

To evaluate the capability of BMGs in nuclear fusion reactor environments, He mobility in both crystalline and amorphous forms of two BMGs was investigated. Both $\text{Zr}_{52.5}\text{Cu}_{17.9}\text{Ni}_{14.6}\text{Al}_{10}\text{Ti}_5$ and $\text{Cu}_{60}\text{Zr}_{20}\text{Hf}_{10}\text{Ti}_{10}$ BMGs were fabricated at Oak Ridge National Laboratory (ORNL) by an arc melting procedure in an argon atmo-

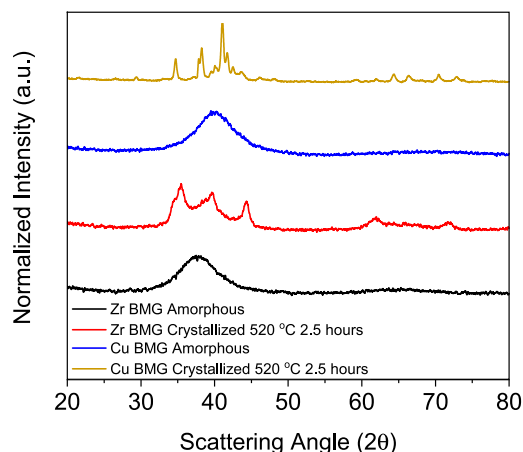


Fig. 1. XRD patterns of the amorphous and crystallized Zr and Cu BMGs.

sphere using a mixture of base metals with the following purities: 99.5% Zr, 99.99% Cu, 99.99% Ni, 99.99% Al, 99.99% Hf, and 99.99% Ti. The alloys were then remelted and drop cast in a Zr-gettered helium atmosphere. XRD characterization of the drop cast rod confirmed the material to be fully amorphous.

After fabrication, BMG samples were cut into rectangular bars with linear dimensions of 3 mm × 2 mm × 6 mm. A subset of the samples were heated in a sealed and evacuated quartz tube at 520 °C for 2.5 hours (ramp rate of 20 °C/min.) at ORNL to induce partial crystallization. To minimize any potential oxidation of the BMGs, Zr sponge was added to the tube before sealing. The amorphous and crystallized BMG samples were then mechanically polished using colloidal silica. To verify the phase of the samples, powder XRD was performed on the polished samples. The XRD measurements were performed at the Joint Institute for Advanced Materials (JIAM) Diffraction Facility, located at the University of Tennessee. A PANalytical Empyrean diffractometer equipped with a Xe proportional detector was employed for the characterization. The X-ray consisted of a Cu beam with a K-alpha wavelength of 1.54 Å and the diffraction angle 2θ ranged between 20–80 degrees. Fig. 1 displays the resulting XRD patterns, and as can be seen for both BMGs, the amorphous samples exhibited a broad hump, while the partially crystallized samples that were produced by thermal annealing displayed distinct diffraction peaks in the pattern. In addition to the first set of samples, supplementary annealing of a second set of samples (dimensions of 3 mm × 2 mm × 10 mm) were performed in a furnace located in Los Alamos National Laboratory (LANL) at 520 °C for 2.5 hours, under a vacuum pressure of 9×10^{-8} torr. XRD characterization also confirmed their partially crystallized structure.

The room temperature He implantations were carried out at the Ion Beam Materials Laboratory (IBML) located in LANL. A 200 kV Varian ion implanter with a chamber pressure of 3×10^{-6} torr was used to perform the He implantations. To study the role of He concentration on the diffusion of He in BMGs, the samples were implanted by He ions with two fluence values of 2×10^{15} ions/cm² and 5×10^{15} ions/cm². From here onwards, the values of 2×10^{15} ions/cm² and 5×10^{15} ions/cm² will be denoted as ϕ_1 and ϕ_2 , respectively. These fluence values were selected to minimize bubble formation in the BMGs since visible bubbles are known to typically form in other monolithic crystalline and amorphous materials at fluences greater than ϕ_2 [21–26]. Moreover, for a more robust analysis on He behavior, two complementary techniques involving NRA and TDS, were used to evaluate He diffusion and outgassing behavior. For the TDS experiment, $^4\text{He}^+$ ion implantations with two fluences ϕ_1 and ϕ_2 , were used. For the NRA experiment, the im-

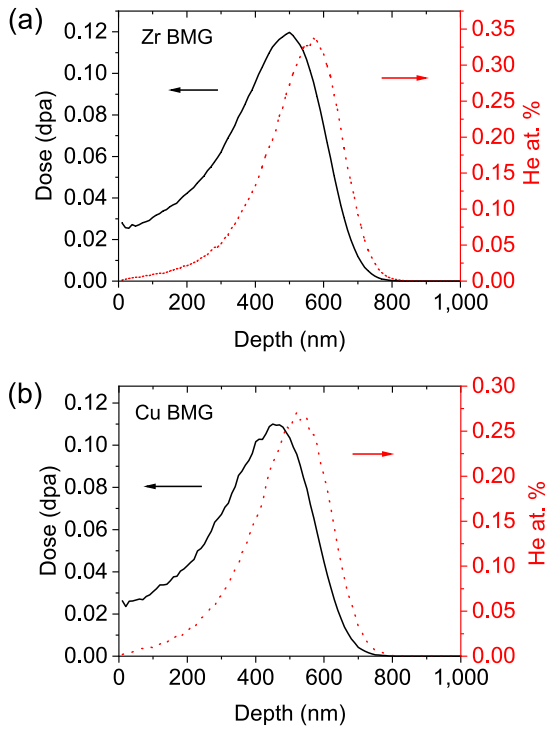


Fig. 2. The dpa profile (fluence of $\phi_2 = 5 \times 10^{15} \text{ cm}^{-2}$) and corresponding at. % He versus depth for the (a) Zr BMG and (b) Cu BMG. Both graphs were obtained from SRIM 2013 simulation using quick Kinchin-Pease calculations.

plantation was performed using $^3\text{He}^+$ ions with only the highest fluence value, ϕ_2 . For all of the He implantations, an ion energy of 150 keV was used.

An example of the damage and He depth profiles for both the Zr and Cu BMGs, as a function of depth for 150 keV energy and ϕ_2 fluence, are displayed in Figs. 2(a)–(b). The depth dependent dpa, corresponding He concentration, and the ion range were estimated using SRIM 2013 in the Quick Kinchin-Pease Mode [27,28]. The ion range for the 150 keV He ions was estimated to be 570 nm and 540 nm for the Zr and Cu BMG, respectively. For this calculation, a displacement threshold energy (E_d) of 40 eV was assumed for all the elements comprising both BMGs. For the Zr BMG, the peak damage and peak He concentration at $\phi_2 = 5 \times 10^{15} \text{ cm}^{-2}$ were estimated to be roughly 0.12 dpa and 0.34 at.%, respectively. For the Cu BMG, these values corresponded to 0.11 dpa and 0.27 at.%, respectively.

The He depth profile was measured using NRA on the ^3He implanted samples using a 3 MV NEC Pelletron tandem accelerator at the ion beam materials laboratory (IBML) at LANL. A deuterium beam with an energy of 575 keV (spot size of $2 \times 2 \text{ mm}^2$) was chosen to overlap the implanted He depth profile over the intrinsic resonance cross section distribution of $^3\text{He}(d,p)^4\text{He}$ reaction centered around the deuterium energy of 430 keV [29,30]. To maximize the detection sensitivity, the sample normal was tilted 60° from the incident beam direction and the Si detector with 2 mm thickness and a large solid angle of $\sim 0.087 \text{ sr}$ was located at 100° in reference to the beam direction. The beam charge collection was done directly from the target, which is biased at 75 V in reference to a current integrator to suppress secondary electron emissions from the target during the measurement. A total charge of 60 μC was used to collect each NRA spectrum. A total error of $\sim 10\%$ was estimated for the NRA experiment. These uncertainties are related to the D-beam charge collection, solid angle measurement, stopping power data among different specimens and reaction yield (proton particles) counting statistics error. To induce the thermal diffusion of He, some of the as-implanted samples were annealed

at different conditions. The annealing temperatures ranged from 250 to 600°C and heating times varied from 15 minutes to 24 hours. The temperature of 250°C was used since it is below the glass transition temperature (393°C for the Zr BMG and 481°C for the Cu BMG [31,32]) while 600°C was used since it is well below the melting point of the BMGs (800°C for the Zr BMG and 916°C for the Cu BMG [31,33]). Samples were heated in a furnace with a ramp rate of $20^\circ\text{C}/\text{min}$ and vacuum pressure of $\sim 10^{-8}$ torr.

The SIMNRA simulation code was implemented to obtain the He depth profile from the NRA raw data. The energy spectrum corresponding to 575 keV deuteron energy were fitted to obtain the helium depth profile of the as-implanted and annealed amorphous and crystallized BMGs. The depth profile was numerically integrated to determine the amount of He remaining in the sample after thermal annealing. For more information on the SIMNRA code, please refer to Refs. [34–38]. The estimated depth resolution for our current ion beam geometry is larger than $1 \mu\text{m}$ based on DEPTH calculation [39], which is significantly larger than the maximum depth of the implanted He profile. As a consequence, only retained helium levels integrated over a depth interval of $\sim 1 \mu\text{m}$ were obtained from the NRA tests.

Additionally, TDS experiments were performed to derive the atomic level activation energies of He migration in the amorphous and crystallized BMG samples. The TDS experiments were performed in the Low Activation Materials Development and Analysis (LAMDA) facility [40] in ORNL. As compared to the NRA experiment, the higher sensitivity of the TDS method allows for the determination of the approximate activation energies for He migration in the BMGs. The as-implanted samples were placed in a quartz tube which was heated by a Thermo Scientific Lindberg tube furnace [41]. The specimens were heated to 770°C with a constant heating rate of $0.4^\circ\text{C}/\text{s}$. During heating, the sample temperature was monitored by using a type K thermocouple located $\sim 5 \text{ mm}$ away from the sample's top surface. To reduce the He background to a level of approximately $2 \times 10^{10} \text{ He/s}$, the base pressure of the system was held at approximately $\sim 1 \times 10^{-8}$ torr. The maximum temperature used for these experiments was based on the melting temperature (T_m) of the Zr BMG since it is lower than that for the Cu BMG ($T_m = 916^\circ\text{C}$ Cu BMG [31]). The maximum temperature for the experiment was kept below $0.97 T_m$ of the Zr BMG as to avoid melting the alloys and possibly damaging the instrument. The released helium was captured via a quadrupole mass spectrometer that was calibrated using a Vacuum Technology Incorporated (VTI) standard helium leak. The ultra-high base vacuum of the thermal desorption chamber (4×10^{-8} torr), provides a very low helium background at a level of 5×10^{-14} ampere, as recorded by the mass spectrometer. Assuming that the He desorption follows a first order kinetic dissociation model, one can calculate the activation energies that are associated with desorption events by using the following equation [41]:

$$\ln\left(\frac{\beta}{T^2}\right) = \ln\left(\frac{fk_B}{T}\right) - \frac{E}{k_B T} \quad (1)$$

where f is the Debye frequency (10^{13} s^{-1} [42]), T is the temperature associated with the desorption peak, E is the activation energy associated with the desorption events, k_B is Boltzmann's constant, and β is the heating rate.

To verify if crystallization and/or bubble formation occurred in the BMG during He implantation and post-implantation annealing experiments, limited TEM characterization was performed. TEM observations at both over- and under-focus conditions were also used to enhance He bubble visibility. The Zr BMG was chosen to perform the TEM analysis due to its relatively lower crystallization temperature as compared to the Cu BMG. The TEM characterization was conducted on the as-cast and partially crystallized Zr BMG that were annealed at 250°C for 15 min., using a Hitachi

HF3300 high resolution TEM-STEM in the Electron Microscopy Laboratory (EML) at LANL. The electron transparent lamellae were prepared (also at the EML) using a FEI Nova 200 Dual-Beam SEM/FIB (Thermo Fisher Scientific, Hillsboro, OR, USA) in which trenching and initial thinning with 30 keV Ga ions was initially performed. To remove the ion induced surface damage, samples were polished using a gradually reduced ion energy down to 2 keV.

3. Results

Figs. 3(a)–(b) show the underfocused TEM bright field (BF) and corresponding selected area diffraction (SAD) images for the amorphous and crystalline Zr BMG specimens. The TEM analysis was conducted on the sample implanted at the highest fluence ($\phi_2 = 5 \times 10^{15} \text{ cm}^{-2}$) in order to assess whether bubble formation could be induced. As discussed earlier, the post-implantation annealing temperature of 250 °C for 15 minutes was chosen because we wanted to keep the samples below the glass transition temperature (T_g) (393 °C [32]) of the alloy. The key points that can be surmised from Figs. 3(a)–(b) are as follows. Firstly, no crystallization of the amorphous phase took place during He implantation at a fluence of $5 \times 10^{15} \text{ cm}^{-2}$ and post-annealing temperature of 250 °C as represented by the well-defined halo in SAD image in Fig. 3(a). Secondly, no amorphization of the crystalline phase took place, as can be seen from the respective SAD images in Fig. 3(b). Thirdly, no He bubbles after irradiation to a fluence of $5 \times 10^{15} \text{ cm}^{-2}$ (3×10^3 appm) with appreciable size (within the TEM resolution limit of ~1 nm) was observed in either of the samples when annealed up to 100 °C below the T_g .

Figs. 4(a)–(b) compare the integrated retained helium levels obtained via NRA for the as-implanted samples at a fluence of $5 \times 10^{15} \text{ cm}^{-2}$ and after post-implantation annealing (250 °C – 600 °C) for the amorphous and crystallized Zr BMG specimens. The integrated retained helium values were calculated by numerically integrating the NRA data over the analyzed depth region of ~0 to 1 μm . It was found that the values were constant within the error of the instrument. The results indicate that for both forms of the Zr BMG that were annealed up to a temperature of 600 °C, there was no detectable outdiffusion of He (or the loss of He was within the percentage error of the instrument). From these results, it can be inferred that there was no appreciable helium release or diffusion observed in either the amorphous or crystallized alloy form for the investigated annealing conditions. Figs. 5(a)–(b) shows similar results for the He implanted amorphous and crystallized Cu BMG sample annealed up to 355 °C, indicating that He diffusion and release (if any) were not measurable by the NRA experimental setup used here. The NRA experimental geometry was designed to

maximize the He detection sensitivity rather than to optimize the depth resolution. Interestingly, the integrated He content and the peak He depth measured by NRA, as displayed in Figs. 4 and 5, are consistent with the implanted He fluence and the SRIM-predicted peak He depth that are shown in Fig. 2.

Figs. 6(a)–(b) compares the results of the TDS He desorption spectra and cumulative He desorption per unit surface area for the amorphous and crystallized Zr BMG specimens that were implanted with 150 keV He ions to the lower fluence of ϕ_1 . Since He release was not observed during the NRA experiments, it was decided to perform the TDS tests up to higher temperatures. Therefore, the TDS experiments were conducted from room temperature to temperatures approaching the melting point of the alloys ($0.85 - 0.97 T_m$). Figs. 6(c)–(d) presents the same results as Figs. 6(a)–(b), but for the higher fluence of ϕ_2 . As an aside, a corresponding energy scale is displayed on the top horizontal axis of all the graphs shown in Figs. 6(a)–(d), where the values correspond to the temperature scale presented on the bottom axis. The energies were calculated using Eq. 1 [41].

Concerning Fig. 6(a), the helium that was released from the amorphous Zr BMG sample is represented by different peaks at different temperatures. This type of pattern indicates that He was being released from a variety of different trapping sites during heating. For instance, there was a moderate helium desorption plateau for the amorphous Zr BMG sample at temperatures ranging from 380 to 447 °C. This desorption is marked as peak 0 in Fig. 6(a). The center of this peak corresponds to a He release activation energy of 1.98 eV. A sharp peak marked as peak I was found at ~467 °C (2.17 eV) and is thought to be associated with the desorption of He that occurs during crystallization of the amorphous alloy. For reference, the reported crystallization temperature of the Zr BMG is 452 °C [33] and is marked by the dotted line in the figure. The part of the curve marked as peak II begins at ~680 °C (2.85 eV) and exhibits an incompletely developed major desorption peak. In contrast, the crystallized sample shows a broad and extremely low helium desorption spectrum that occurred for temperatures ranging from 270 to 640 °C. Significant helium desorption in the crystallized Zr BMG begins at 675 °C and continues until the maximum measurement temperature is reached.

Fig. 6(b) displays the cumulative desorption fluence, as derived from Fig. 6(a), for the amorphous and crystallized Zr BMG samples so that the cumulative He desorption at different temperatures could be directly compared. For temperatures ranging from 380 to ~700 °C, there was more He release in the amorphous form, as compared to the crystallized Zr BMG sample. However, once the temperature exceeded 700 °C, both the amorphous and crystallized forms exhibited the majority of the He release. Furthermore,

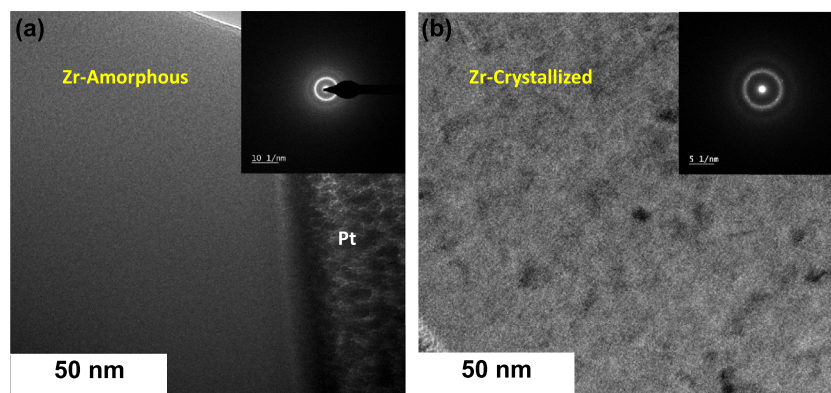


Fig. 3. TEM BF and corresponding SAD images for the He implanted ($5 \times 10^{15} \text{ cm}^{-2}$) (a) amorphous Zr BMG (b) crystallized Zr BMG. Both samples were annealed after the He implantation at a temperature of 250 °C for 15 minutes.

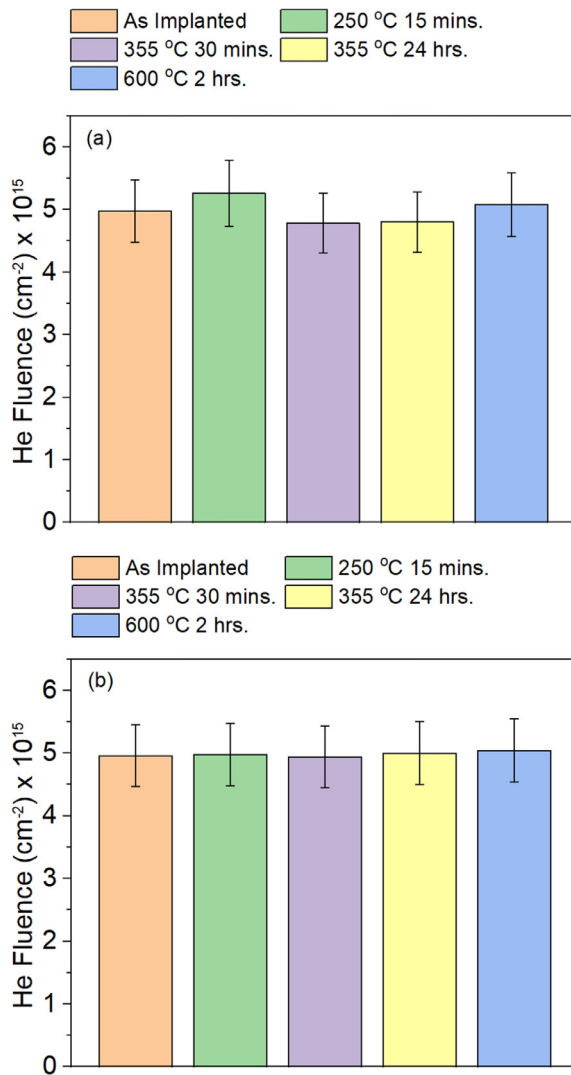


Fig. 4. The integrated helium values, as obtained by the NRA, for the as-implanted (150 keV He , $5 \times 10^{15} \text{ cm}^{-2}$) and annealed samples (a) amorphous Zr BMG and the (b) crystallized Zr BMG after annealing at different temperatures and times.

relatively more helium desorbed from the crystallized BMG sample. The total desorbed helium from the crystallized BMG is 3.3 times that from amorphous samples for this low implantation fluence condition, ϕ_1 .

Fig. 6(c) presents the TDS results for both forms of the Zr BMG that was irradiated to the high fluence of ϕ_2 . The trend in Fig. 6(c) is similar to the low fluence implantation case shown in Fig. 6(a) except that the desorption plateau ("peak 0" at 380 to 447°C) for amorphous Zr BMG is absent. The sharp peak I for fluence ϕ_2 was also centered around 467°C (2.17 eV) and can only be observed for the amorphous form of the Zr BMG, indicating that this peak is associated with crystallization. For the crystallized sample (Fig. 6(c)), there is a broad helium desorption regime that occurred for temperatures ranging from 368 to 490°C of which the helium desorption flux is very low, similar to the low fluence case. Also, similar to the low fluence case, both samples exhibit significant helium desorption starting from $\sim 700^\circ\text{C}$ up to the maximum measurement temperature of 770°C . The main peak II was centered at 756°C (3.03 eV) for the amorphous sample and the helium desorption spectrum of the crystallized samples has a peak temperature of 762°C . Like the low fluence case, more pronounced helium desorption also occurred in the crystallized sample (as compared to

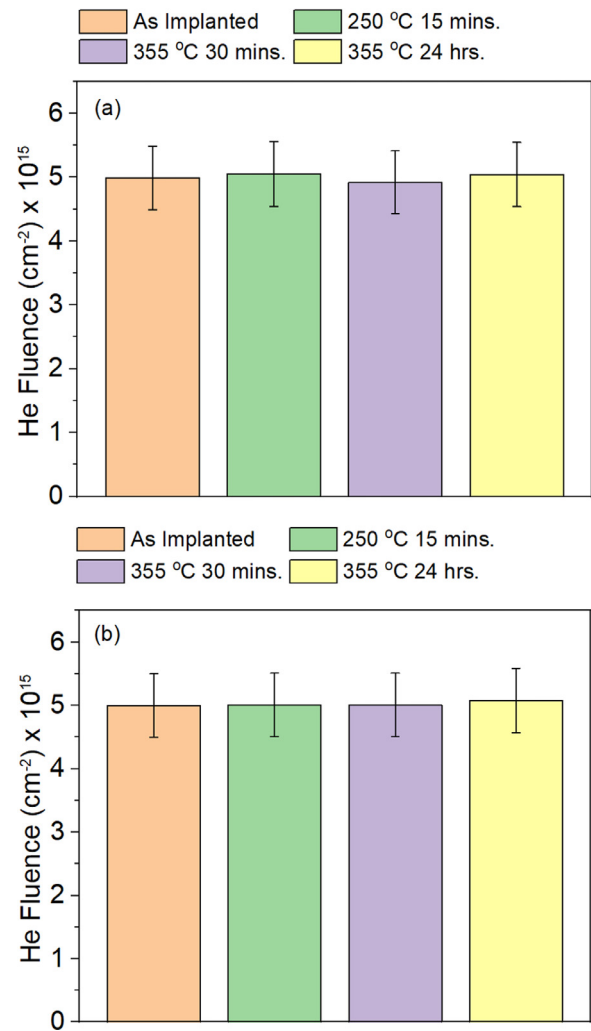


Fig. 5. The integrated helium values, as obtained by the NRA, for the as-implanted (150 keV He , $5 \times 10^{15} \text{ cm}^{-2}$) and annealed samples (a) amorphous Cu BMG and the (b) crystallized Cu BMG after annealing at different temperatures and times.

the amorphous sample) for this high temperature desorption peak II.

Fig. 6(d) shows the cumulative desorption fluence, as determined from Fig. 6(c), for the Zr BMG that was irradiated to the high fluence ϕ_2 . Similar to Fig. 6(b), the regions of increasing fluence correspond to the peaks in Fig. 6(c). However, unlike Fig. 6(b), more He release occurred in the crystallized sample than in the amorphous Zr BMG for temperatures ranging from 380°C to $\sim 700^\circ\text{C}$. It should also be mentioned that once the temperature exceeded 700°C , both samples exhibited a similar increase in the desorbed fluence up to a maximum value of $\sim 5 \times 10^{14} \text{ cm}^{-2}$.

Figs. 7(a)–(b) present a comparison of the total percentage of desorbed He from the TDS results for the amorphous and crystallized Zr BMG irradiated to fluences ϕ_1 and ϕ_2 after annealing up to $\sim 770^\circ\text{C}$. The total He release percentage was determined by integrating the flux data with respect to temperature, and then dividing by the ramp rate. A key observation from Figs. 7(a)–(b) is that the sample which was implanted to the higher fluence ϕ_2 released substantially less He ($\sim 10\%$ of implanted amount) as compared to the sample implanted to the lower fluence ϕ_1 . Importantly, this was observed in both the amorphous and crystalline forms. The amount of desorbed He was $\sim 10\%$ of the implanted value for both the amorphous and crystallized Zr BMG specimens at the higher fluence ϕ_2 . At the lower fluence ϕ_1 , less helium was

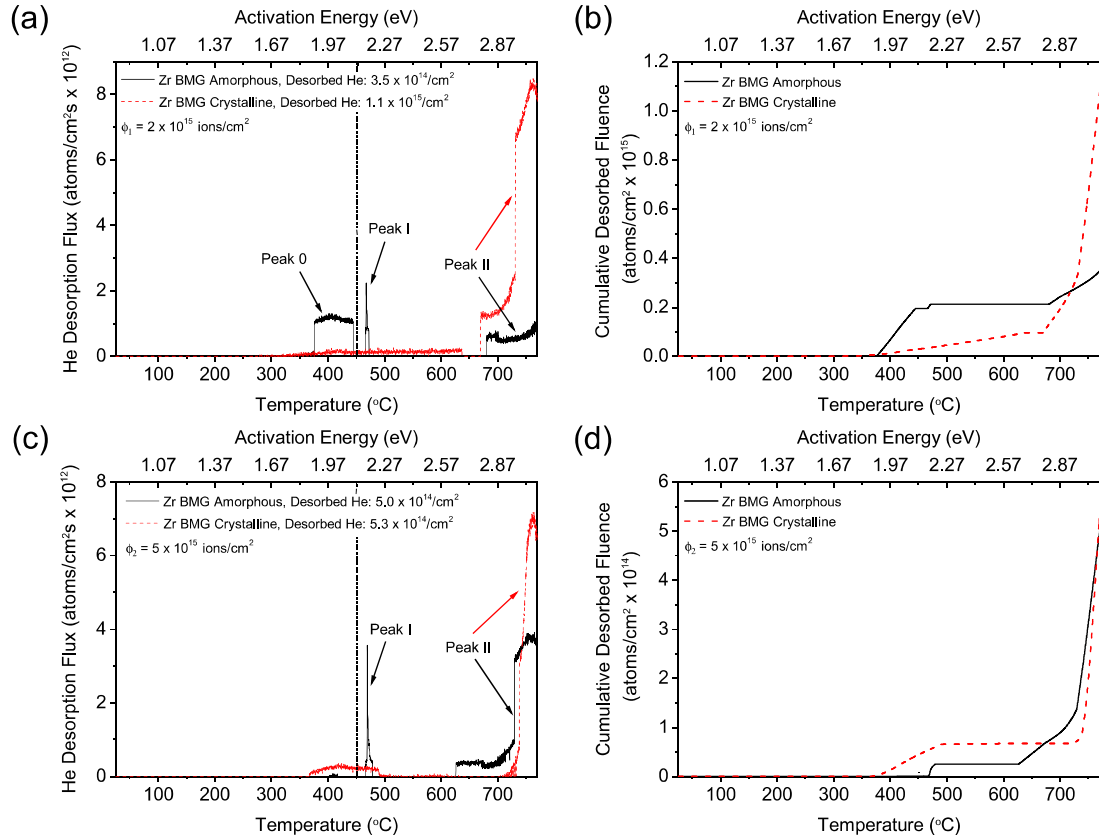


Fig. 6. TDS spectra of the 150 keV He implantation of the (a) amorphous and crystalline Zr BMG ($2 \times 10^{15} \text{ cm}^{-2}$), (b) corresponding cumulative desorbed fluence for figure (a), (c) amorphous and crystalline Zr BMG ($5 \times 10^{15} \text{ cm}^{-2}$), and (d) corresponding cumulative desorbed fluence for figure (c). The dotted vertical lines in Figs. 6(a), 6(c) represent the crystallization temperature of the Zr BMG (452 °C [33]).

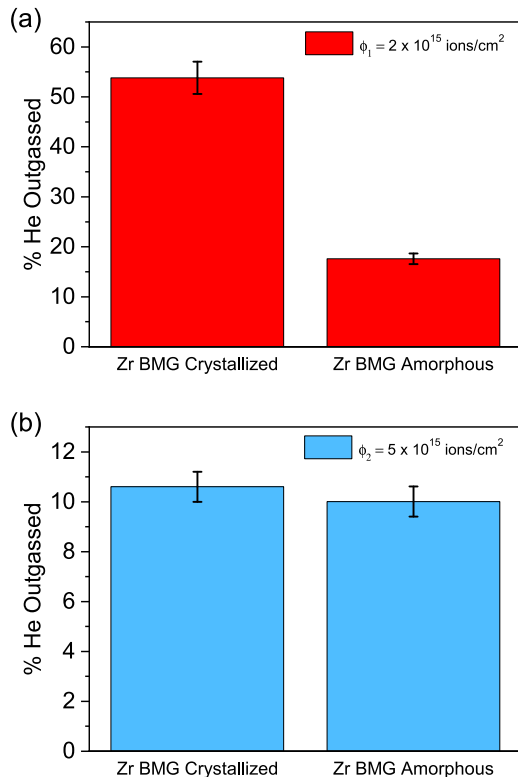


Fig. 7. Cumulative helium outgassing values up to $\sim 770^\circ\text{C}$, as calculated by TDS, in the amorphous and crystallized Zr BMG implanted to (a) $2 \times 10^{15} \text{ ions/cm}^2$ and (b) $5 \times 10^{15} \text{ ions/cm}^2$.

desorbed from the amorphous sample ($\sim 15\%$) compared to crystallized BMG ($\sim 50\%$).

Figs. 8(a)–(b) compare the results of the He desorption spectra from the amorphous and crystallized Cu BMG specimens that were implanted with 150 keV He ions to the high fluence ϕ_2 . For this implantation fluence value, both the amorphous and crystallized samples exhibited a small amount of He release below 500°C . For instance, a broad plateau centered around $\sim 420^\circ\text{C}$ can be observed for both the amorphous and crystallized forms, which corresponded to an activation energy of 2.03 eV. Similar to the Zr BMG specimens, only amorphous Cu BMG specimen showed a sharp peak centered around $\sim 505^\circ\text{C}$, which corresponds to an activation energy of 2.29 eV. This peak is most likely attributed to the He release during crystallization of the alloy that occurs around $\sim 509^\circ\text{C}$ [31]. For both types of specimens, the main peak II that corresponded to the maximum desorbed helium was centered at 710°C (2.90 eV) and 730°C (2.96 eV) for the crystallized and amorphous samples, respectively.

Fig. 9 summarizes the total percentage of He that desorbed during the TDS testing from the amorphous and crystallized Cu BMG irradiated to the high fluence of ϕ_2 . The crystalline specimen released about twice as much He as compared to the amorphous sample, i.e., $\sim 7\%$ vs. $\sim 3.5\%$. However, both specimens overall exhibited relatively low He desorption up to the maximum examined annealing temperature of $\sim 770^\circ\text{C}$. For this high fluence implantation case, the magnitude of the He desorption fraction was comparable to (smaller than) the He release observed in the corresponding TDS results of Zr BMG samples implanted to the highest fluence (see Fig. 7(b)).

Fig. 10 displays the XRD results for the initially amorphous and crystalline Zr BMG samples implanted to the two different fluences

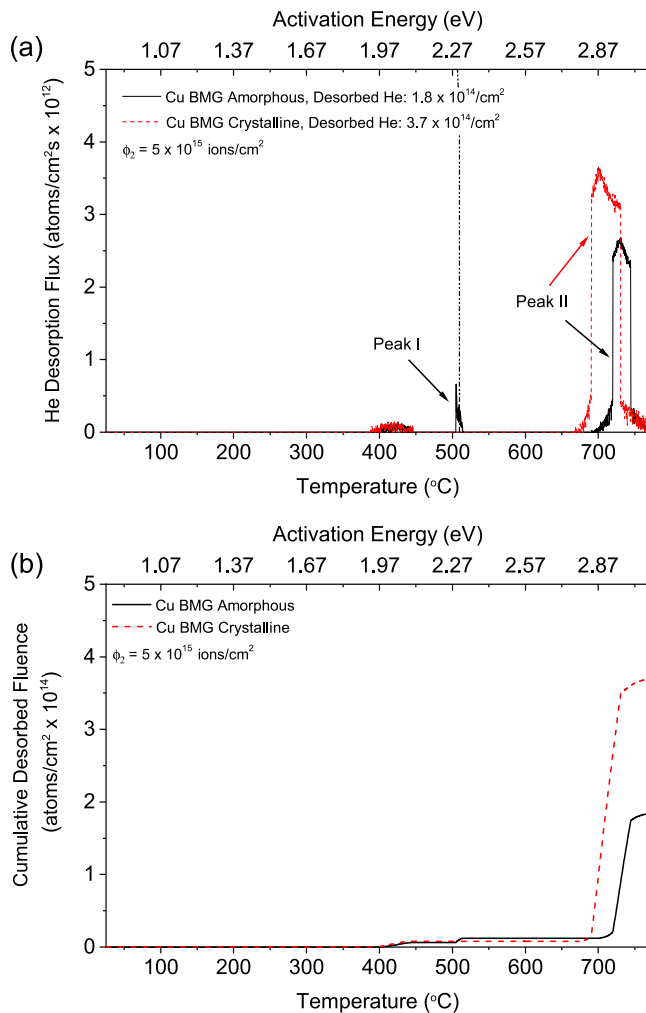


Fig. 8. The (a) TDS spectra of the 150 keV He implantation (5×10^{15} ions/cm²) of the amorphous and crystalline Cu BMG and the (b) corresponding cumulative desorbed fluence. The dotted vertical line in Fig. 8(a) represents the crystallization temperature of the Cu BMG (509 °C [31]).

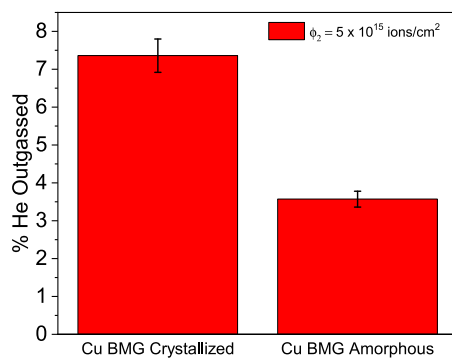


Fig. 9. Cumulative helium outgassing values up to ~770°C in the crystallized and amorphous Cu BMG samples (implanted He fluence of 5×10^{15} cm⁻²).

following the TDS annealing characterization (where all samples became crystallized). As can be observed, all the specimens displayed multiple crystalline diffraction peaks. This result confirms that the originally amorphous samples crystallized during the TDS annealing measurements, which is also linked to the sharp He release peak observed at 467 °C.

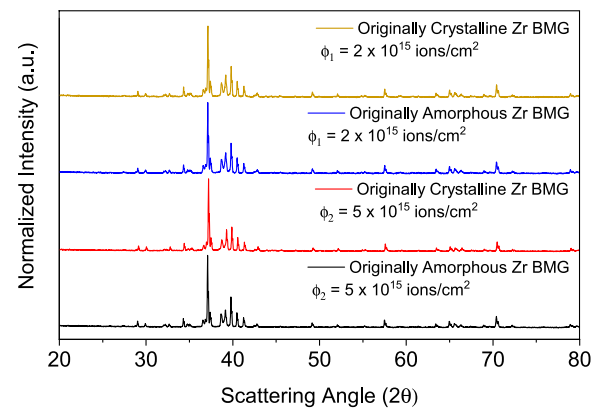


Fig. 10. Post TDS structural examination which features the XRD patterns for the crystallized Zr BMG specimens in which they were exposed to He fluences of 2×10^{15} cm⁻² and 5×10^{15} cm⁻².

4. Discussion

As part of an assessment of the viability of BMGs in nuclear fusion reactor environments, we examined the He diffusion in both crystalline and amorphous forms of Zr and Cu based BMGs with good mechanical properties. To derive the atomic level activation energies of He migration, the He fluence values used in this study were kept well below the typical threshold value of He bubble formation for materials. The lack of TEM-visible bubbles for the Zr BMG irradiated to the highest examined helium fluence ($\phi_2 = 5 \times 10^{15}$ cm⁻²) is in agreement with prior studies on monolithic crystalline and amorphous materials implanted near room temperature [21–26]. The subsequent thermally activated He diffusion and release measurements were carried out using two techniques, namely TDS and NRA methods.

Typically, Fick's Law can be applied to the diffusion-induced change in the full width half maximum (FWHM) implantation profile to calculate the apparent activation energies for He diffusion [30,37]. However, in our case, the He depth profiles obtained from the NRA for different annealing temperatures revealed no perceptible He migration below 600 °C. In other words, no significant change in the integrated retained helium values (Figs. 4 and 5) occurred after annealing up to 600 °C. Therefore, no He diffusion activation energies could be derived from the NRA measurements. However, approximate activation energies for He migration could be determined using the higher sensitivity TDS method to detect He release (Figs. 6 and 8). Limited He release, i.e., much less than 10% of the implanted amount, was observed at temperatures well below 600 °C using the TDS technique (estimated activation energy of ~2.0 eV). However, this relatively low release was followed by the main helium release at a temperatures higher than 600 °C. Importantly, the lack of any significant outgassing at temperatures below 600 °C during the TDS experiment further substantiates the findings of the NRA experiment. The activation energy corresponding to the majority of helium release at a temperature higher than 600 °C is estimated by TDS to be around 2.87 to 3.03 eV for the different BMGs.

The TDS profile for the amorphous BMGs clearly shows different dominant He desorption peaks, which are labeled as 0, I, and II in Fig. 6(a) and I and II in Fig. 8(a). Each peak corresponds to a different He associated migration mechanism, which is predominantly active at different temperatures. Standard solute diffusion in crystalline metals and ceramics is typically associated with conventional defects such as vacancies. In such materials, the desorption peak at low temperatures is typically attributed to the mobility of small He-vacancy clusters [43]. In our case, a similar peak is

observed that is represented by desorption peak 0. It is important to recall that BMGs contain non-conventional defects such as quasi-vacancies (low atomic density regions) [44,45], which appears to play a similar role to vacancies. Hence, the desorption peak 0 is likely attributed to these types of defects.

For the Cu and Zr BMGs, crystallization is known to occur at $\sim 509^\circ\text{C}$ and $\sim 452^\circ\text{C}$, respectively [31,33]. The sharp desorption peak I in the Cu and Zr BMGs (see Figs. 6(a) and 8(a)) occurs near their crystallization temperatures, which suggests that the sudden release of He is likely due to the structural changes that occur during crystallization at that temperature. The desorption peak II, which constitutes the major He release, appears to be at the same temperature for both the amorphous and crystallized BMGs. Depending on the BMG alloy, initial structural state (amorphous vs. crystallized) and He implantation fluence (Figs. 7, 9), 3.5 to 50% of the implanted He is cumulatively released by this temperature, which is very close to the melting point of the alloys ($0.85\text{--}0.97 T_m$). Generally, studies have reported that the He release in typical crystalline materials can begin as low as $-0.2 - 0.5 T_m$, depending upon different implantation condition such as fluence and temperature [36,46,47]. But based on the present study, it appears that for these BMGs He is not released until temperatures much higher than $0.5 T_m$ for the investigated implantation conditions.

Furthermore, the He release is highly dependent on the fluence or quantity of implanted He. As summarized in Fig. 7, the desorbed He fraction for the initially amorphous Zr BMG samples is about 50% larger (10% vs. 15% desorption fraction) for the lower fluence ($\phi_1 = 2 \times 10^{15} \text{ cm}^{-2}$) sample compared to the higher fluence ($\phi_2 = 5 \times 10^{15} \text{ cm}^{-2}$) case. An even greater variation in desorbed He fraction (10% vs. 50%) was observed for the high fluence vs. low fluence case for crystallized Zr BMG. Larger He releases have generally been observed in crystalline materials for lower implanted He fluences compared to higher fluences [38,47]. This behavior has been attributed to smaller He-vacancy cluster sizes at low implantation fluences, with corresponding increased mobility at lower temperatures compared to the larger average He-vacancy cluster sizes produced at higher implant fluences. For the higher fluence cases, higher temperature is needed to either induce migration of the He-vacancy cluster or to promote dissociation of the He-vacancy cluster. In our study, the majority of the He is released at very high temperatures ($0.85\text{--}0.97 T_m$) in all the sample conditions. The presence of this predominant high-temperature release peak, irrespective of the fluences and different sample forms, indicates that He defect complexes are very stable and immobile in BMGs. The lack of observable broadening in the profiles by NRA up to 600°C provides further evidence that He defects are immobile up to intermediate temperatures. The lack of peak broadening and lower mobility of He in both of the BMGs during annealing at temperatures below T_g may be due to the immobilization of He in the free volume regions of the alloy.

There were observable differences in the He desorption peaks for the amorphous and crystalline Zr BMG samples. This effect of structure on the desorption peaks is understandable since the peaks are usually associated with He release from various trapping sites that reach a given activation energy during the heating sequence [48]. It should also be mentioned that sharp peaks found in the amorphous samples at elevated temperatures, as opposed to the broad and overlapping peaks observed at lower temperatures, are caused by a re-distribution of helium atoms due to recrystallization [48,49]. The wide desorption peaks in the figures are interpreted to be associated with multiple types of trapping sites in the material. In the samples, the physical mechanism of trapping helium could possibly be due to either vacancy-like defects (atom-sized-holes) produced during irradiation or a self-trapping mechanism of interstitial helium precipitation [50]. Finally, the crystalline Zr BMG, as compared to the amorphous Zr BMG, that was irradi-

ated to a fluence of ϕ_1 exhibited very low desorption of helium until the temperature reached values exceeding 700°C .

The overall comparison in terms of the net He release between the amorphous and crystallized structure of the BMGs cannot be performed as Peak II is not completely formed. Furthermore, the most important part of the TDS curve is what happens below $\sim 450^\circ\text{C}$. We have already studied the behavior $\sim 300^\circ\text{C}$ above the crystallization temperature. It should be noted that significant He release doesn't begin until temperatures $>250^\circ\text{C}$ above the upper use temperature for this BMG (its crystallization temperature).

In addition to BMGs, other studies have examined He diffusion in disordered materials. For instance, Mizuguchi et al. studied the He migration in SiOC glasses with different compositions [51]. Here, a-SiOC thin films with $\text{SiO}_2\text{:SiC}$ ratios of 2:1 (SiO_2 -rich), 1:1 (equiatomic), and 1:2 (SiC-rich) were implanted with 120 keV He ions to a fluence of approximately 10^{13} cm^{-2} (90 at.% He). Electron diffraction characterization revealed that the SiO_2 -rich and equiatomic forms of the SiOC glasses exhibited superior He swelling resistance as compared to the SiC-rich specimen. This enhanced resistance to swelling was attributed to the relatively larger size of network voids (3.5 to 3.7 nm) formed by connecting the $\text{SiO}_x\text{C}_{4-x}$ tetrahedra, which are much larger than the diameter of the He atom. Furthermore, Su et al. reported an average He migration energy of 0.14 eV in SiOC [12], which is comparable to migration energies in some transition metals [52]. This rapid He diffusion in the SiOC was ascribed to an interstitial-like diffusion mechanism in a relatively open continuous random network structure [11,12]. Altemose examined the He permeation rate in 20 different oxide glasses [53]. The permeation of He was found to increase with increasing molar concentration of glass network formers (glass forming oxides). This trend was attributed to the formation of chain-like glassy networks with openings sufficiently large to enable permeation of small gas atoms or molecules.

In summary, the He diffusion and desorption for the two investigated BMGs following room temperature He implantation to peak concentrations of $\sim 1,100$ to $3,500$ appm was remarkably sluggish up to temperatures approaching 700°C ($\sim 0.90 T_m$). Somewhat higher He desorption was observed for crystallized BMG compared to the initially amorphous implanted specimens. The observed low He permeability for the two investigated BMGs may be problematic for potential fusion energy applications of these materials, since He generated in the materials from fusion neutron induced transmutation reactions may serve as nucleation sites for the development of porosity and accompanying volumetric swelling. This low He permeability in the two investigated BMGs is different from the rapid He permeation observed in other amorphous materials such as SiOC. This reduced diffusion of He in the BMGs may be due to the trapping of He in the free volume regions of the glass.

5. Conclusions

This study focused on the helium behavior in BMGs, which are potential candidates in nuclear fusion systems. Based on the NRA results, it can be concluded that the He did not diffuse in any of the room temperature implanted specimens even after annealing at temperatures ranging from 250 to 600°C . This lack of diffusion was attributed to an insufficient concentration of hole defects that can facilitate atomic diffusion as well as the trapping of He in free volume sites. Furthermore, TEM analysis revealed that bubbles did not form in the glass after He implantation to the highest investigated fluence of $\phi_2 = 5 \times 10^{15} \text{ cm}^{-2}$ (peak implanted He concentration of $\sim 3,500$ appm) and annealing at 250°C for 15 minutes. Therefore, it is possible the He atoms coalesced to form atomic-scale He-vacancy clusters with sizes that were below the resolution of the TEM. On the other hand, the lack of peak broadening during the NRA testing may have been related to issues with the

limited depth resolution of the solid-state detector apparatus. For the TDS experiments, He was found to exhibit minor off-gassing behavior at temperatures below the glass crystallization temperature that is thought to be associated with sets of distinct sites where gas is trapped. Overall, the TDS results indicate He is highly stable (immobile) in the two investigated metallic glasses and does not exhibit pronounced migration in BMG until temperatures exceed a threshold temperature of $\sim 600^\circ\text{C}$, well above the glass crystallization temperature.

Declaration of Competing Interest

The authors declare that they have no known competing financial interests or personal relationships that could have appeared to influence the work reported in this paper.

CRediT authorship contribution statement

J. Brechtel: Conceptualization, Formal analysis, Investigation, Methodology, Visualization, Writing - original draft. **S. Agarwal:** Conceptualization, Investigation, Methodology, Writing - original draft, Writing - review & editing. **X. Hu:** Formal analysis, Investigation, Methodology, Resources, Writing - review & editing. **D. Chen:** Investigation. **M. Chancey:** Investigation. **H. Bei:** Resources. **Y.Q. Wang:** Conceptualization, Funding acquisition, Investigation, Methodology, Resources, Writing - review & editing. **S.J. Zinkle:** Conceptualization, Funding acquisition, Supervision, Writing - original draft, Writing - review & editing.

Acknowledgements

This research was sponsored in part by the Office of Fusion Energy Sciences, U.S. Department of Energy under contract DE-AC05-00OR22725 with UT-Battelle, LLC and grant # DE-SC0006661 with the University of Tennessee. This work was performed, in part, at the Center for Integrated Nanotechnologies, an Office of Science User Facility operated for the U.S. Department of Energy (DOE), Office of Science. Los Alamos National Laboratory, an affirmative action equal opportunity employer, is operated by Los Alamos National Security, LLC, for the National Nuclear Security Administration of the U.S. Department of Energy under Contract No. DE-AC52-6NA25396.

Supplementary materials

Supplementary material associated with this article can be found, in the online version, at doi:10.1016/j.jnucmat.2020.152617.

References

- [1] E.E. Bloom, R.W. Conn, J.W. Davis, R.E. Gold, R. Little, K.R. Schultz, D.L. Smith, F.W. Wiffen, Low activation materials for fusion applications, *J. Nucl. Mater.* 122 (1–3) (1984) 17–26.
- [2] K. Ehrlich, E.E. Bloom, T. Kondo, International strategy for fusion materials development, *J. Nucl. Mater.* 283 (2000) 79–88.
- [3] S.J. Zinkle, Fusion materials science: Overview of challenges and recent progress, *Physics of Plasmas* 12 (5) (2005).
- [4] E.E. Bloom, S.J. Zinkle, F.W. Wiffen, Materials to deliver the promise of fusion power - progress and challenges, *J. Nucl. Mater.* 329 (2004) 12–19.
- [5] C.L. Smith, The need for fusion, *Fusion Engineering and Design* 74 (1–4) (2005) 3–8.
- [6] S.-H. Li, J.-T. Li, W.-Z. Han, Radiation-induced helium bubbles in metals, *Materials* 12 (7) (2019) 1036.
- [7] R.W. Cahn, Materials science - Aluminum-based glassy alloys, *Nature* 341 (6239) (1989) 183–184.
- [8] P. Chaudhari, D. Turnbull, Structure and properties of metallic glasses, *Science* 199 (4324) (1978) 11–21.
- [9] A.L. Greer, Metallic glasses, *Science* 267 (5206) (1995) 1947–1953.
- [10] W.J. Weber, R.C. Ewing, C.A. Angell, G.W. Arnold, A. N.Cormack, J.M. Delaye, D.L. Griscom, L.W. Hobbs, A. Navrotsky, D.L. Price, A.M. Stoneham, M.C. Weinberg, Radiation effects in glasses used for immobilization of high-level waste and plutonium disposition, *J. Mater. Res.* 12 (8) (1997) 1946–1978.
- [11] Q. Su, S. Inoue, M. Ishimaru, J. Gigax, T.Y. Wang, H.P. Ding, M.J. Demkowicz, L. Shao, M. Nastasi, Helium irradiation and implantation effects on the structure of amorphous silicon oxycarbide, *Sci Rep* 7 (2017) 8.
- [12] Q. Su, H.P. Ding, L. Price, L. Shao, J.A. Hinks, G. Greaves, S.E. Donnelly, M.J. Demkowicz, M. Nastasi, Rapid and damage-free outgassing of implanted helium from amorphous silicon oxycarbide, *Sci Rep* 8 (2018) 9.
- [13] S.J. Zinkle, A. Moslang, T. Muroga, H. Tanigawa, Multimodal options for materials research to advance the basis for fusion energy in the ITER era, *Nucl. Fusion* 53 (10) (2013) 13.
- [14] X.X. Mei, B. Wang, C. Dong, F.Q. Gong, Y.N. Wang, Z.G. Wang, Anti-irradiation performance against helium bombardment in bulk metallic glass ($\text{Cu}_{47}\text{Zr}_{45}\text{Al}_8$)_{98.5\text{Y}_{1.5}}, *Nucl. Instrum. Methods Phys. Res. Sect. B-Beam Interact. Mater. Atoms* 307 (2013) 11–15.
- [15] B. Wang, X.X. Mei, W.J. Hou, Y.N. Wang, Z.G. Wang, C. Dong, Behavior of high resistance to He^{2+} induced irradiation damage in metallic glass, *Nucl. Instrum. Methods Phys. Res. Sect. B-Beam Interact. Mater. Atoms* 312 (2013) 84–89.
- [16] W.J. Hou, X.X. Mei, Z.G. Wang, Y.N.A. Wang, Resistance to He^{2+} irradiation damage in metallic glass $\text{Fe}_{80}\text{Si}_{7.43}\text{B}_{12.57}$, *Nuclear Instruments & Methods in Physics Research B* 342 (2015) 221–227.
- [17] B. Wang, X.X. Mei, H.R. Zhang, W.J. Hou, Y.N. Wang, Z.G. Wang, C. Dong, Resistance to He^{2+} induced irradiation damage in metallic glass $\text{Zr}_{64}\text{Cu}_{17.8}\text{Ni}_{10.7}\text{Al}_{7.5}$, *J. Nucl. Mater.* 444 (1–3) (2014) 342–348.
- [18] A. Manuaba, F. Paszti, L. Pogany, M. Fried, E. Kotai, G. Mezey, T. Lohner, I. Lovas, L. Pocs, J. Gyulai, Comparative-study on $\text{Fe}_{32}\text{Ni}_{36}\text{Cr}_{14}\text{P}_{12}\text{B}_8$ metallic-glass and its polycrystalline modification bombarded by 2000-keV helium-ions with high fluence, *Nuclear Instruments & Methods in Physics Research* 199 (1–2) (1982) 409–419.
- [19] R. Lontas, X.W. Gu, E.G. Fu, Y.Q. Wang, N. Li, N. Mara, J.R. Greer, Effects of helium implantation on the tensile properties and microstructure of $\text{Ni}_{73}\text{P}_{27}$ metallic glass nanostructures, *Nano Letters* 14 (9) (2014) 5176–5183.
- [20] K. Unlu, D.H. Vincent, He-3 behavior in some nickel-based amorphous-alloys, *Nucl. Sci. Eng.* 110 (4) (1992) 386–393.
- [21] K.Q. Chen, S.H. Yang, Z.G. Wang, J.G. Sun, J.M. Quan, L.W. Li, Y.M. Sun, The analysis of microstructure of helium bubbles in 316L SS induced by 3.02 MeV He ion irradiation, *J. Nucl. Mater.* 191 (1992) 737–741.
- [22] P.B. Johnson, D.J. Mazey, Gas-bubble superlattice formation in bcc metals, *J. Nucl. Mater.* 218 (3) (1995) 273–288.
- [23] A.M. Robinson, P.D. Edmondson, C. English, S. Lozano-Perez, G. Greaves, J.A. Hinks, S.E. Donnelly, C.R.M. Grovenor, The effect of temperature on bubble lattice formation in copper under in situ He ion irradiation, *Scr. Mater.* 131 (2017) 108–111.
- [24] Y. Watanabe, S. Nanao, A. Kohyama, Radiation damage in $\text{Fe}_{80}\text{B}_{20}$ amorphous alloy irradiated with helium ions, *J. Nucl. Mater.* 122 (1–3) (1984) 743–747.
- [25] S.J. Zinkle, Effect of H and He irradiation on cavity formation and blistering in ceramics, *Nucl. Instrum. Methods Phys. Res. Sect. B-Beam Interact. Mater. Atoms* 286 (2012) 4–19.
- [26] H. Chen, Y. Hai, R. Liu, Q. Lei, L. Ye, J. Xu, G. Wang, W. Yin, L. Yan, X. Zhou, The microstructure and mechanical properties of He^+ ion irradiated $\text{Zr}_{55}\text{Cu}_{30}\text{Al}_{10}\text{Ni}_5$ bulk metallic glass, *Intermetallics* 104 (2019) 52–58.
- [27] R.E. Stoller, M.B. Toloczko, G.S. Was, A.G. Certain, S. Dwaraknath, F.A. Garner, On the use of SRIM for computing radiation damage exposure, *Nucl. Instrum. Methods Phys. Res. Sect. B-Beam Interact. Mater. Atoms* 310 (2013) 75–80.
- [28] J.F. Ziegler, M.D. Ziegler, J.P. Biersack, SRIM - The stopping and range of ions in matter (2010), *Nuclear Instruments & Methods in Physics Research B* 268 (2010) 1818–1823.
- [29] S.M. Myers, Nuclear-reaction analysis of helium-3 and tritium in tritium-exposed austenitic steels, United States, 1987, p. 11.
- [30] S. Agarwal, Helium mobility in advanced nuclear ceramics, *Universite Paris-Sud, France* (2014).
- [31] Z.X. Wang, D.Q. Zhao, M.X. Pan, W.H. Wang, T. Okada, W. Utsumi, Formation and crystallization of CuZrHfTi bulk metallic glass under ambient and high pressures, *J. Phys.-Condens. Matter* 15 (35) (2003) 5923–5932.
- [32] A.G. Perez-Bergquist, H. Bei, K.J. Leonard, Y. Zhang, S.J. Zinkle, Effects of ion irradiation on $\text{Zr}_{52.5}\text{Cu}_{17.9}\text{Ni}_{14.6}\text{Al}_{10}\text{Ti}_5$ (BAM-11) bulk metallic glass, *Intermetallics* 53 (2014) 62–66.
- [33] X. Gu, L.Q. Xing, T.C. Hufnagel, Glass-forming ability and crystallization of bulk metallic glass ($\text{Hf}_{52}\text{Zr}_{18}\text{Cu}_{17.9}\text{Ni}_{14.6}\text{Al}_{10}\text{Ti}_5$), *J. Non-Cryst. Solids* 311 (1) (2002) 77–82.
- [34] M. Mayer, SIMNRA User's Guide, Max-Planck-Institut für Plasmaphysik, Garching, Germany, 1997.
- [35] M. Mayer, SIMNRA User's Guide, Max-Planck-Institut für Plasmaphysik, Garching, Germany, 2017.
- [36] S. Agarwal, A. Bhattacharya, P. Trocellier, S.J. Zinkle, Helium induced microstructure damage, nano-scale grain formation and helium retention behaviour of ZrC, *Acta Mater* 163 (2019) 14–27.
- [37] S. Agarwal, P. Trocellier, S. Vaubailon, S. Miro, Diffusion and retention of helium in titanium carbide, *J. Nucl. Mater.* 448 (1) (2014) 144–152.
- [38] S. Agarwal, P. Trocellier, D. Brimbal, S. Vaubailon, An experimental study of helium diffusion and helium induced microstructural evolution in ion implanted polycrystalline titanium nitride, *Acta Mater* 121 (2016) 1–14.
- [39] E. Szilagy, Energy spread in ion beam analysis, *Nucl. Instrum. Methods Phys. Res. Sect. B-Beam Interact. Mater. Atoms* 161 (2000) 37–47.
- [40] C.M. Parish, N.A.P.K. Kumar, L.L. Snead, P.D. Edmondson, K.G. Field, C. Silva, A.M. Williams, K. Linton, K.J. Leonard, Lamda: Irradiated-materials microscopy at Oak Ridge National Laboratory, *Microsc. Microanal.* 21 (2015) 1003–1004.

- [41] X. Hu, K.G. Field, S. Taller, Y. Katoh, B.D. Wirth, Impact of neutron irradiation on thermal helium desorption from iron, *J. Nucl. Mater.* 489 (2017) 109–117.
- [42] G.S. Was, *Fundamentals of Radiation Materials Science*, Springer Science & Business Media, New York, 2007 1 ed..
- [43] S. Kawano, F. Kano, C. Kinoshita, A. Hasegawa, K. Abe, Effect of weld thermal cycle, stress and helium content on helium bubble formation in stainless steels, *J. Nucl. Mater.* 307 (2002) 327–330.
- [44] A.K. Tyagi, M.P. Macht, V. Naundorf, Diffusion coefficients of ^{63}Ni in $\text{Fe}_{40}\text{Ni}_{40}\text{B}_{20}$ metallic glass, *Acta Metallurgica et Materialia* 39 (4) (1991) 609–617.
- [45] F. Faupel, W. Frank, M.P. Macht, H. Mehrer, V. Naundorf, K. Ratzke, H.R. Schober, S.K. Sharma, H. Teichler, Diffusion in metallic glasses and supercooled melts, *Rev. Mod. Phys.* 75 (1) (2003) 237–280.
- [46] P. Trocellier, S. Agarwal, S. Miro, A review on helium mobility in inorganic materials, *J. Nucl. Mater.* 445 (1) (2014) 128–142.
- [47] P. Jung, K. Schroeder, Diffusion and agglomeration of helium in FCC metals, *J. Nucl. Mater.* 155 (1988) 1137–1141.
- [48] O. El-Atwani, C.N. Taylor, J. Frishkoff, W. Harlow, E. Esquivel, S.A. Maloy, M.L. Taheri, Thermal desorption spectroscopy of high fluence irradiated ultra-fine and nanocrystalline tungsten: helium trapping and desorption correlated with morphology, *Nucl. Fusion* 58 (1) (2018) 14.
- [49] C.N. Taylor, M. Shimada, B.J. Merrill, Deuterium retention and blistering in tungsten foils, *Nuclear Materials and Energy* 12 (2017) 689–693.
- [50] A.K. Tyagi, R.V. Nandedkar, Helium irradiation of Ni-(Zr or Nb) metallic glasses: Blistering, flaking and bubble formation, *Journal of Nuclear Materials* 132 (1) (1985) 62–69.
- [51] S. Mizuguchi, S. Inoue, M. Ishimaru, Q. Su, M. Nastasi, Compositional effects on radiation tolerance of amorphous silicon oxycarbide, *J. Nucl. Mater.* 518 (2019) 241–246.
- [52] C. Gonzalez, R. Iglesias, Migration mechanisms of helium in copper and tungsten, *J. Mater. Sci.* 49 (23) (2014) 8127–8139.
- [53] V.O. Altemose, Helium Diffusion through Glass, *J. Appl. Phys.* 32 (7) (1961) 1309–1316.
- [54] Y. Wang, K. Zhang, Y. Feng, Y. Li, W. Tang, Y. Zhang, B. Wei, Z. Hu, Mechanism of local hardening in metallic glass during He ion irradiation, *Materialia* 11 (2020) 100691.